
# Estimation Algorithm for Current and Temperature of Field Winding in Electrically Excited Synchronous Machines with High-Frequency Brushless

# Estimation Algorithm for Current and Temperature of Field Winding in Electrically Excited Synchronous Machines with High-Frequency Brushless Exciters

Junfei Tang, *Student Member*, *IEEE*, Yujing Liu, *Senior Member*, *IEEE*, and Stefan Lundberg, *Member, IEEE*

***Abstract* – Electrically excited synchronous machines (EESMs) have become one of the potential alternatives to permanent magnet synchronous machines (PMSMs) in electric vehicles (EVs) to avoid rare-earth materials. Utilizing high-frequency brushless exciters for rotor excitation is a promising choice to reduce friction losses and maintenance effort and cost. However, with the usage of brushless exciters, the field current and temperature cannot be measured directly. In this paper, an algorithm is proposed to dynamically estimate the field current as well as the field winding temperature. The dc-link current is utilized as a feedback to correct the estimation. The performance of the estimation algorithm is initially evaluated in simulations and then verified by experimental measurements in a prototype. Based on the estimation algorithm, closed-loop control of the field current is developed and verified experimentally.**

*Index Terms* – Electrically excited synchronous machines, wound field synchronous machines, electric vehicles, estimation algorithm, field excitation.

## I. Introduction

Electrically excited synchronous machines (EESMs), also known as wound field synchronous machines, have become an alternative to permanent magnet synchronous machines (PMSMs) in electric vehicles (EVs). This is mainly attributed to the absence of rare-earth materials in EESMs [1] [2] [3]. Instead of being excited by permanent magnets, field windings in the rotor are employed in EESM. Therefore, the excitation can be controlled by adjusting the field current [4] [5]. Consequently, it becomes possible to achieve a high starting torque and a wide field weakening range [6]. Moreover, by using high-frequency signal injection in the field winding, sensorless control independent from the saliency ratio of the machine can be achieved [7].

Concerning the field excitation topologies of the EESM-based drive systems, an extensive summary of different technologies has been presented in [8]. In static topologies, silicon-controlled rectifiers are used to convert three-phase power to dc power and then the power is fed into the field winding through brushes and slip rings. These are mainly used in generators with high power ratings. In integrated topologies, the exciter is integrated into the machine structure. Space harmonics can be coupled to the coils in the rotor, and the power is routed into the field winding using an integrated rectifier. In EV applications, where a compact design is required, the high-frequency brushless topology becomes an interesting alternative [9] [10] [11] [12] [13] [14] [15] [16]. A general schematic diagram of the high frequency brushless excitation system is shown in Fig. 1. A rotating transformer is introduced between the power supply and the field winding. The primary side is mounted on the stator frame whereas the secondary side is mounted on the rotor. An H-bridge inverter with phase-shift control delivers power to the primary side, and the power is transferred to the secondary side through an air gap. A rotating diode rectifier converts ac power to dc power, and then the current flows to the field winding. Using this technology, the power is transferred through an air gap with no mechanical contact. Consequently, friction loss is reduced, and maintenance to clear dust and replace brushes is not required.

However, introducing brushless excitation to electrical machines also brings other technical challenges. For instance, the field winding is physically inaccessible after assembly. Therefore, the feedback of the field current for closed-loop control is not an easy task. The heat generated by the field winding copper loss exhibits an additional problem. Hence, the estimation of the field winding temperature to protect the winding from overheating is of particular importance.

To estimate the field current in similar scenarios has been the scope of some previous studies. A current estimation algorithm has been developed in [17] for a wound-rotor synchronous starter-generator with asynchronous brushless exciters. Initially, the rotor currents and voltages of the exciter are estimated, and then the field current is calculated through the parametric average-value model of the rotating rectifier. Capacitive coupling is employed in [18] for brushless power transfer. In capacitive power transfer, there is no shunt path similar to the magnetizing branch in inductive power transfer. This makes the estimation of the field current easier.

The temperature estimation of the rotor windings is a similar challenge for induction machines and doubly-fed induction machines. Extensive studies have been performed in this area. An approach with resistance-based temperature estimation for stator and rotor windings has been investigated in [19]. A reliable thermal protection can be achieved with this algorithm. Using a controllable small dc signal injection, accurate temperature estimation is achieved in [20]. In [21], a high-frequency signal injection method is proposed for the estimation of the rotor winding temperature in doubly-fed induction machines. The estimated error in dynamics is lower than 5°C. A high-frequency model of the rotor copper bar in induction motors is built in [22]. A rotor temperature estimation algorithm is then developed based on this model.

The abovementioned studies have been successful in their

Junfei Tang, Yujing Liu and Stefan Lundberg are with the Department of Electrical Engineering, Chalmers University of Technology, Gothenburg, Sweden (email: junfei.tang@chalmers.se; yujing.liu@chalmers.se; stefan.lundberg@chalmers.se).

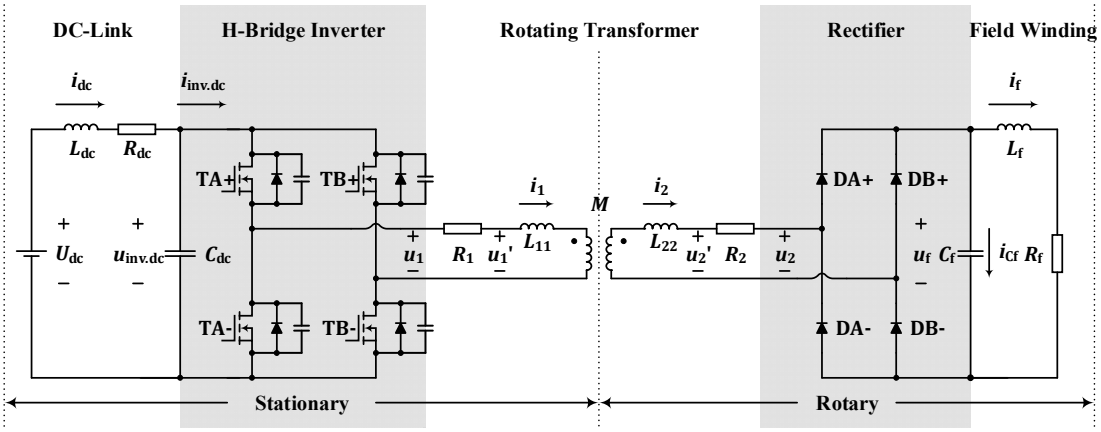


Fig. 1. Schematic diagram of brushless excitation system used in EESM.

specific applications and topologies. However, regarding the excitation topology in traction EESMs, further investigations are required. Due to the large field winding inductance, high-frequency signal injection into the field winding becomes challenging. The field current itself is a dc quantity; therefore, the method using dc signal injection is not applicable here. Additionally, since a compact design is required in traction applications, inductive power transfer seems a more mature technology in this situation.

Therefore, the aim of this study is to develop an online algorithm for the current and temperature estimations of the field winding in traction EESM using high-frequency brushless excitation. With this algorithm assisted, closed-loop field current control and overheating protection of the field winding becomes achievable.

## II. Brushless Excitation System

The brushless excitation system shown in Fig. 1 is modeled mathematically. Then an EESM with brushless excitation is prototyped and the model is validated. Based on the model, the estimation algorithm is proposed in the next chapter.

### A. System Modeling

The system consists of several components, i.e., the dc-link, H-bridge inverter, transformer, rectifier and field winding, as shown in Fig. 1. Each component can be described by a number of equations. A few simplifications are introduced to reduce computational power. The model of the system is developed in [23] and it is briefly summarized as follows.

*1) DC-Link*

The DC-link inductance $L_{\mathrm{dc}}$ and capacitance $C_{\mathrm{dc}}$ are energy storage components. Hence the DC-link current, $i_{\mathrm{dc}}$ together with voltage across the capacitor, $u_{\mathrm{inv.dc}}$ are counted as states. The states can be described as

$$\begin{cases} \dfrac{di_{\mathrm{dc}}}{dt} = \dfrac{U_{\mathrm{dc}} - u_{\mathrm{inv.dc}} - R_{\mathrm{dc}} \cdot i_{\mathrm{dc}}}{L_{\mathrm{dc}}} \\ \dfrac{du_{\mathrm{inv.dc}}}{dt} = \dfrac{i_{\mathrm{dc}} - i_{\mathrm{inv.dc}}}{C_{\mathrm{dc}}} \end{cases}, \tag{1}$$

where $i_{\mathrm{inv.dc}}$ is the current going into the inverter. $i_{\mathrm{inv.dc}}$ can be described as

$$i_{\mathrm{inv.dc}} = i_1 \cdot (s_{\mathrm{TA+}} - s_{\mathrm{TB+}}), \tag{2}$$

where $i_1$ is the transformer primary current, $s_{\mathrm{TA+}}$ and $s_{\mathrm{TB+}}$ are the upper leg switching signals of Phase A and B respectively.

*2) H-Bridge Inverter*

The terminal voltage of the inverter $u_1$ can be described as

$$u_1 = u_{\mathrm{inv.A}} - u_{\mathrm{inv.B}}, \tag{3}$$

where $u_{\mathrm{inv.A}}$ and $u_{\mathrm{inv.B}}$ are the terminal voltages of Phase A and B respectively. $u_{\mathrm{inv.A}}$ and $u_{\mathrm{inv.B}}$ are decided by switching actions

$$u_{\mathrm{inv.A}} = \begin{cases} \dfrac{u_{\mathrm{inv.dc}}}{2} - R_{\mathrm{ds}} \cdot i_1 & s_{\mathrm{TA+}} = 1 \quad s_{\mathrm{TA-}} = 0 \\ R_{\mathrm{ds}} \cdot i_1 - \dfrac{u_{\mathrm{inv.dc}}}{2} & s_{\mathrm{TA+}} = 0 \quad s_{\mathrm{TA-}} = 1 \end{cases}, \tag{4}$$

$$u_{\mathrm{inv.B}} = \begin{cases} \dfrac{u_{\mathrm{inv.dc}}}{2} - R_{\mathrm{ds}} \cdot i_1 & s_{\mathrm{TB+}} = 1 \quad s_{\mathrm{TB-}} = 0 \\ R_{\mathrm{ds}} \cdot i_1 - \dfrac{u_{\mathrm{inv.dc}}}{2} & s_{\mathrm{TB+}} = 0 \quad s_{\mathrm{TB-}} = 1 \end{cases}, \tag{5}$$

where $R_{\mathrm{ds}}$ is the drain-to-source resistance of the MOSFET, $s_{\mathrm{TA-}}$ and $s_{\mathrm{TB-}}$ are the lower leg switching signals of Phase A and B respectively.

*3) Rotating Transformer*

The current derivatives of the two sides of the transformer can be described as

$$\frac{di_1}{dt} = -L_{22} \cdot \frac{u_1 - R_1 \cdot i_1}{M^2 - L_{11} \cdot L_{22}} + M \cdot \frac{u_2 + R_2 \cdot i_2}{M^2 - L_{11} \cdot L_{22}}, \tag{6}$$

$$\frac{di_2}{dt} = -M \cdot \frac{u_1 - R_1 \cdot i_1}{M^2 - L_{22} \cdot L_{11}} + L_{11} \cdot \frac{u_2 + R_2 \cdot i_2}{M^2 - L_{22} \cdot L_{11}}, \tag{7}$$

where $i_2$ and $u_2$ are the transformer secondary current and voltage respectively, $R_1$ and $R_2$ are the ac resistances of the primary and secondary windings respectively, $L_{11}$ and $L_{22}$ are the primary and secondary self-inductances respectively, and $M$ is the mutual inductance between both sides. The resistance variation due to temperature is neglected since in practice the temperature variation of transformer windings is

negligible compared with that of the field winding.

*4) Rectifier*

A capacitor $C_\mathrm{f}$ is connected to the output of the rectifier. This is to mitigate the high-frequency oscillations between the parasitic capacitance of the diodes and the transformer inductances. The capacitor current $i_{C_\mathrm{f}}$ can be described as

$$i_{C_\mathrm{f}} = |i_2| - i_\mathrm{f}, \tag{8}$$

where $i_\mathrm{f}$ is the field current. Additionally, $u_2$ is decided by the field voltage $u_\mathrm{f}$ and the diode forward voltage drop $u_\mathrm{D}$

$$u_2 = \mathrm{sign}(i_2) \cdot (u_\mathrm{f} + 2 \cdot u_\mathrm{D}). \tag{9}$$

*5) Field Winding*

The field winding is modeled by field winding resistance $R_\mathrm{f}$, inductance $L_\mathrm{f}$, and rectifier output capacitance $C_\mathrm{f}$. The derivatives of the capacitor voltage and inductor current are

$$\begin{aligned} \frac{du_\mathrm{f}}{dt} &= \frac{i_{C_\mathrm{f}}}{C_\mathrm{f}}, \\ \frac{di_{L_\mathrm{f}}}{dt} &= \frac{u_\mathrm{f} - R_\mathrm{f} \cdot i_{L_\mathrm{f}}}{L_\mathrm{f}}. \end{aligned} \tag{10}$$

The field resistance at temperature $T$ is scaled from the resistance at temperature 20℃

$$R_\mathrm{f}(\mathrm{T}) = R_\mathrm{f}(20℃) \cdot [1 + \alpha_\mathrm{Cu} \cdot (T - 20)], \tag{11}$$

where $\alpha_\mathrm{Cu}$ is the temperature coefficient of copper resistance.

## B. Experimental Prototype

A traction EESM for mild hybrid application was prototyped. The parameters of the machine and the brushless excitation system are listed in TABLE I and TABLE II respectively. The switching frequency is 100 kHz and the blanking time is 100 ns. This gives a maximum duty cycle of 0.99. The excitation system is shown in Fig. 2. Flux transfers through air gap in the axial direction. Coils formed by Litz wires were inserted into the transformer cores made of ferrite, and then solidified to the core using Epoxy. The ferrite cores were then supported by aluminum cases, and a rectifier PCB was attached to the back of the transformer secondary side.

The test setup is shown in Fig. 3. The switching signals were generated in a digital signal processor (DSP). The machine was disassembled during the test so that the field current could be measured by probes. The field winding temperature was measured by two PT100 sensors inserted into the winding with 180 degrees shift in space. The PT100 measurement shown in this paper is the mean value of the readings of the two sensors. A drawback of utilizing PT100 sensors is that the thermal contact resistance between the sensors and the copper strands would always introduce an offset in temperature measurement. As an alternative, the field winding temperature can be determined by the resistance of the field winding. This resistance can be calculated by the field current and voltage measured by the probes. Calibrations were performed to make sure that the temperature determined by the field current and voltage measurements was consistent with the PT100 measurement in steady state. This is to view the trend of temperature change instead of measuring the absolute temperature precisely. It should also be pointed out that the coupling between the primary and secondary coils is not affected by the relative speed between the two transformer sides. Hence although the experiments in this work were performed when the machine was dissembled, the results are still valid when the rotor is rotating after the assembly.

TABLE I MACHINE PARAMETERS

| Parameter | Value | Unit | Condition |
|---|---|---|---|
| Machine active length | 80 | mm | |
| Machine stator outer diameter | 120 | mm | |
| Field current at peak operation | 18 | A | |
| RMS stator current at peak operation | 500 | A | |
| Field winding resistance | 5.08 | Ω | dc, 20℃ |
| Field winding inductance | 130 | mH | |
| DC-link voltage | 60 | V | |
| Base speed | 4500 | rpm | |
| Peak power for 30 s | 15 | kW | |

TABLE II BRUSHLESS EXCITATION SYSTEM PARAMETERS

| Parameter | Value | Unit | Condition |
|---|---|---|---|
| DC-link voltage | 60 | V | |
| Inverter MOSFET maximum voltage | 100 | V | |
| Inverter MOSFET maximum current | 300 | A | 25℃ |
| Transformer primary side resistance | 27 | mΩ | |
| Transformer secondary side resistance | 9.5 | mΩ | |
| Transformer primary self-inductance | 2.60 | μH | |
| Transformer secondary self-inductance | 21.85 | μH | |
| Transformer mutual inductance | 6.06 | μH | |
| Rectifier diode threshold voltage | 557 | mV | |
| Rectifier diode conduction resistance | 4.0 | mΩ | |
| Switching frequency | 100 | kHz | |

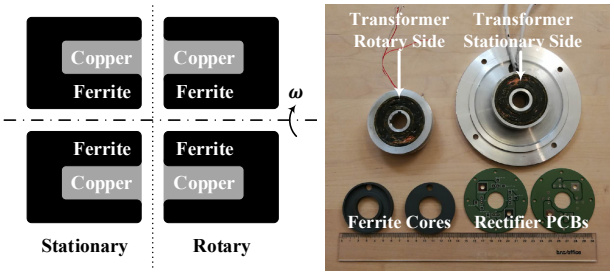


(a) topology with axial excitation (b) transformer, ferrite and rectifier

Fig. 2. Rotary transformer.

## C. Model Validation

The model is implemented in Simulink. Due to the accuracy limitation of the measurement devices, a mismatch exists between the values of the transformer mutual inductance identified from primary and secondary sides, 5.70 μH and 6.23 μH respectively. To decide the true value, the mean of the two was taken and then it was calibrated so that the simulated field current value at the maximum duty cycle (0.99) fits the experimental one. The value presented in TABLE II is the calibrated one, 6.06 μH, and it is within the range of the two

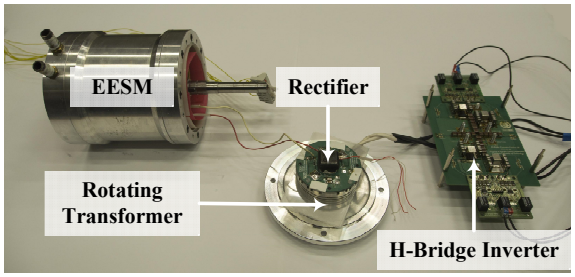


(a)

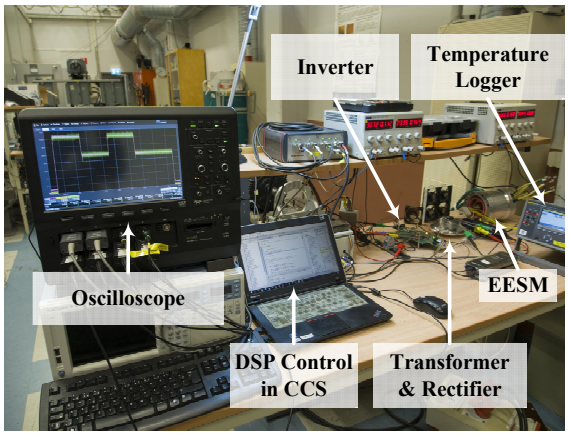


(b)

Fig. 3. Test setup. (a) component connections; (b) test bench.

measured values.

The simulated dc-link and field current rising profiles at duty cycle of 0.99 are compared to those obtained from experiments, as shown in Fig. 4. It can be observed that the simulated curves closely follow the experimental curves. The differences between the two curves in (b) during current rise are probably due to the non-linear behavior of the diodes.

A decrease in the field and dc-link currents due to the field winding temperature variation is observed in Fig. 5 and Fig. 6.

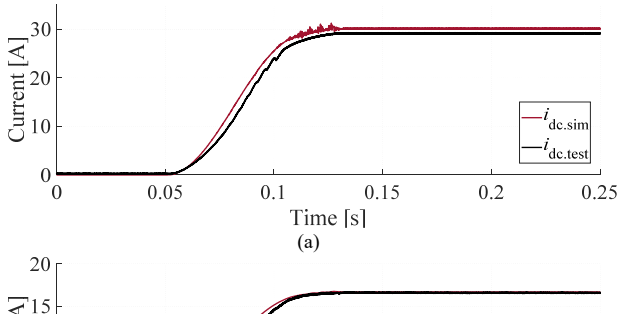


(a)

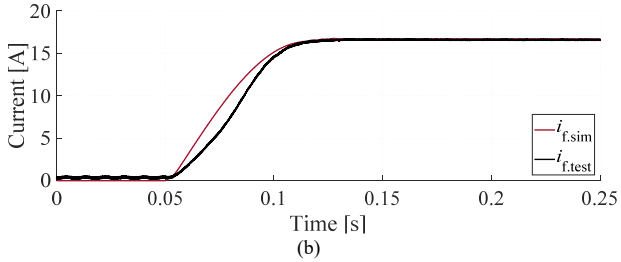


(b)

Fig. 4. Simulated and experimental current transients at 40°C (0.99 duty cycle). (a) dc-link current; (b) field current.

The simulated curves closely follow the experimental curves. However, the dc-link current exhibits a different profile compared to the field current. This can be explained with the assistance of power balance in the system. In steady state, the output power equals the input power multiplying the efficiency

$$U_{\mathrm{dc}} \cdot I_{\mathrm{dc}} \cdot \eta_{\mathrm{tot}} = P_{\mathrm{dc}} \cdot \eta_{\mathrm{tot}} = P_{\mathrm{f}} = I_{\mathrm{f}}^2 \cdot R_{\mathrm{f}}, \qquad (12)$$

where $U_{\mathrm{dc}}$ is the dc-link voltage, $I_{\mathrm{dc}}$ is the dc-link current, $\eta_{\mathrm{tot}}$ is the total efficiency of the system including inverter, transformer and rectifier, $P_{\mathrm{dc}}$ is the dc-link power, $P_{\mathrm{f}}$ is the field winding copper loss, $I_{\mathrm{f}}$ is the field current, and $R_{\mathrm{f}}$ is the field winding resistance. Therefore, the dc-link current is proportional to the square of the field current assuming an almost constant efficiency

$$I_{\mathrm{dc}} = \frac{R_{\mathrm{f}}}{U_{\mathrm{dc}} \cdot \eta_{\mathrm{tot}}} \cdot I_{\mathrm{f}}^2. \qquad (13)$$

This explains why the field current curves between duty cycle 0.0 and 0.5 in Fig. 5 are almost linear whereas within the same duty cycle range the dc-link current curves seem to be quadratic in Fig. 6. The work described in [23] shows that the variation of $\eta_{\mathrm{tot}}$ is around 5% within the duty cycle from 0.2 to 1.0.

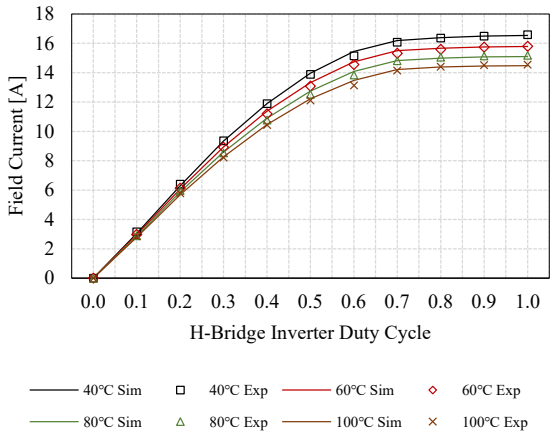


Fig. 5. Field current at 40, 60, 80 and 100°C.

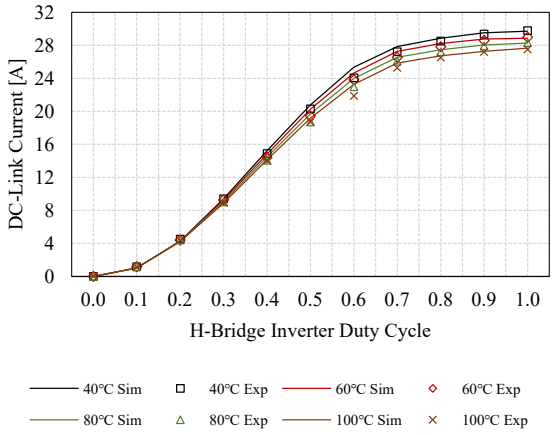


Fig. 6. DC-link current at 40, 60, 80 and 100°C.

## III. Estimation Algorithm

The behavior of the dc-link current versus temperature is monotonic for any given duty cycle higher than zero. This indicates that if the duty cycle is known and the dc-link current can be measured, it is possible to determine the temperature of the field winding. Then with the duty cycle and the temperature, the field current can be estimated. The basic idea of the estimation algorithm is shown in Fig. 7.

From a control system perspective, the input to the excitation system is the duty cycle, and the outputs, i.e. the responses, from the excitation system are the field and the dc-link currents. The dc-link current is measurable, whereas the field current is not. Therefore, an observer can be placed and can run in parallel with the excitation system so that the estimated dc-link current can be compared with the measured one. The error can be fed back to correct the estimation.

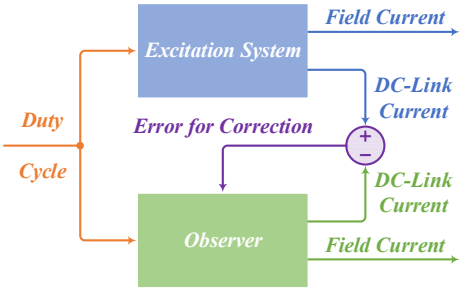


Fig. 7. System modules of the proposed estimation algorithm.

### A. Algorithm Structure

The proposed algorithm can be explained by the detailed schematic diagram shown in Fig. 8. The observer in this algorithm, which runs in parallel with the excitation system, is described by two datasets together with the dynamic response shaping process. These datasets describe the field and dc-link current profiles versus temperature and the duty cycle as shown in Fig. 5 and Fig. 6. The datasets in this algorithm can be either lookup tables or formulas. The formulas can be derived analytically or extracted by curve fitting the simulated or experimental data.

Initially, the algorithm assumes a winding temperature, and the current controller provides a duty cycle. The duty cycle and the assumed winding temperature are fed into the datasets. Then, the estimated values of the steady-state field and dc-link currents are generated. The steady-state estimations are shaped into instantaneous values, through dynamic response shaping processes. The estimated field current is fed into the field current controller while the estimated dc-link current is compared with the measured dc-link current. The error obtained is then used to correct the temperature estimation. Subsequently, with the updated temperature estimation, the field and dc-link current estimations are also updated. Hence the datasets together with the dc-link current and the temperature dynamic response shaping processes form the temperature correction loop. The updates continue until the error between the estimated and measured dc-link currents goes to zero.

### B. Signal Filtering and Ramping

The algorithm requires a stable measurement of the dc-link current. This can be achieved by implementing a moving average of the dc-link current. In this way, high-frequency noise due to electromagnetic interference (EMI) can be filtered out. In this work, an average of 100 samples is applied. It should be pointed out that, moving averaging is one of the techniques used to deal with EMI. On the other hand, this technique is not necessary if other techniques are applied.

However, filtering will introduce a time delay. The measured dc-link current is compared with the estimated dc-link current, which is calculated from the duty cycle. Therefore, the duty cycle needs to be delayed by the same amount of time so that the two signals in comparison are synchronized. This can be realized by adding the same moving average filter in the path through which the duty cycle signal is fed into the algorithm. Additionally, in practice, the duty cycle is ramped in the machine control, so that the back EMF gradually increases, and the stator current controller has enough time to react.

### C. Datasets

Datasets can be described by lookup tables, analytical formulas or formulas extracted by curve fitting of the experimental data. Analytical solutions can be derived if the rectifier output capacitance is high enough to keep the field voltage constant [24]. In this work, the capacitance is not high enough to hold the field voltage constant. However, a comprehensive understanding of the current profile in Fig. 5 and Fig. 6 can be established using analytical solutions.

The amplitude of the fundamental voltage component of the inverter $U_{1\cdot\mathrm{amp}}$ is as follows:

$$U_{1\cdot\mathrm{amp}} = \frac{4}{\pi} U_{\mathrm{dc}} \sin\left(\frac{\pi}{2} d\right), \tag{14}$$

where $d$ is the duty cycle. Assuming that there are no losses, the mean absolute value of the fundamental component on the secondary side of the transformer becomes the field voltage:

$$U_{\mathrm{f}} = \frac{2}{\pi} U_{2\cdot\mathrm{amp}} = \frac{2}{\pi} \frac{N_2}{N_1} U_{1\cdot\mathrm{amp}}. \tag{15}$$

Therefore, the field current can be calculated as follows:

$$I_{\mathrm{f}} = \frac{U_{\mathrm{f}}}{R_{\mathrm{f}}} = \frac{2}{\pi} \frac{N_2}{N_1} \frac{U_{1\cdot\mathrm{amp}}}{R_{\mathrm{f}}} = \frac{8}{\pi^2} \frac{N_2}{N_1} \frac{U_{\mathrm{dc}}}{R_{\mathrm{f}}} \sin\left(\frac{\pi}{2} d\right), \tag{16}$$

where $U_{\mathrm{f}}$ is the field voltage and $\frac{N_2}{N_1}$ is the turns ratio between the primary and secondary coils of the transformer. This explains the profile in Fig. 5 where the $I_{\mathrm{f}}$ curve is in the shape of $\sin\left(\frac{\pi}{2} d\right)$. The dc-link current can be calculated by substituting (16) into (13)

$$I_{\mathrm{dc}} = \frac{32}{\pi^4} \frac{{N_2}^2}{{N_1}^2} \frac{U_{\mathrm{dc}}}{R_{\mathrm{f}}} \frac{1 - \cos(\pi d)}{\eta_{\mathrm{tot}}}. \tag{17}$$

This explains the profile in Fig. 6 where the $I_{\mathrm{dc}}$ curve is in the shape of $[1 - \cos(\pi d)]$.

Again, the analytical solutions derived in (16) and (17) are based on the assumption that the rectifier output capacitance is

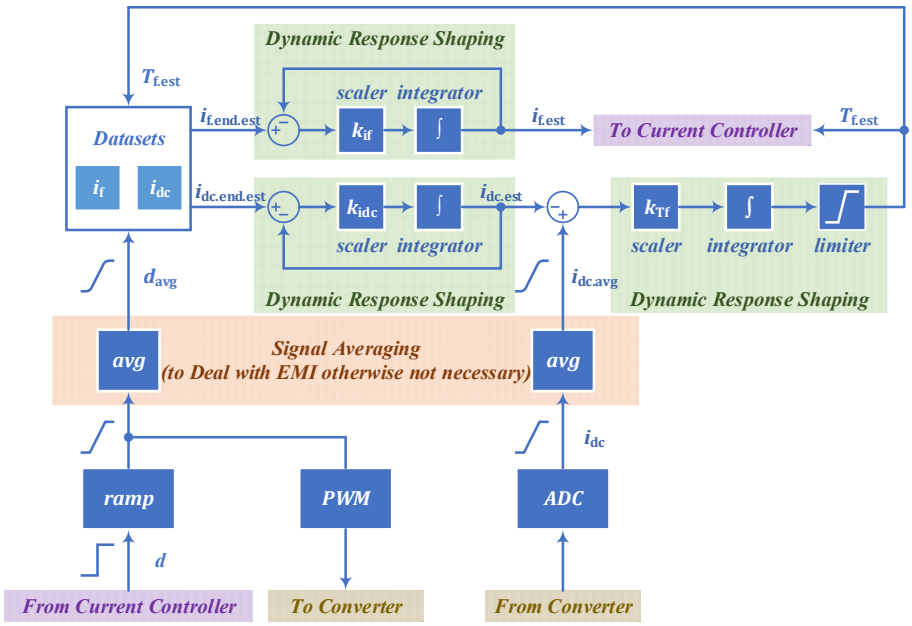


Fig. 8. Illustration of the estimation algorithm.

high enough to keep the field voltage as a pure dc quantity. If this is not true, curve fitting of the experimental data can be applied. In this work, rational polynomial fitting is applied with the following format:

$$I = \frac{p_1 \cdot d^2 + p_2 \cdot d + p_3}{d^2 + q_1 \cdot d + q_2} \Big/ [\alpha \cdot (T_\mathrm{f} - T_{\mathrm{f}\cdot 0}) + 1], \qquad (18)$$

where $I$ represents the field current $I_\mathrm{f}$ or the dc-link current $I_\mathrm{dc}$, $p_1$, $p_2$ and $p_3$ are the coefficients in the numerator, $q_1$ and $q_2$ are the coefficients in the denominator, $\alpha$ is the scaling factor for temperature, $T_\mathrm{f}$ is the field winding temperature, and $T_{\mathrm{f}\cdot 0}$ is the base temperature where $\frac{p_1 \cdot d^2 + p_2 \cdot d + p_3}{d^2 + q_1 \cdot d + q_2}$ is valid.

In this work, because of the differences between experimental and simulation results as compared in Fig. 5 and Fig. 6, the fitting formula extracted from simulation results is be used to simulate the algorithm, whereas the fitting formula extracted from experimental results is used for the experimental verification of the algorithm.

### D. Dynamic Response Shaping

The datasets provide steady-state estimations for the dc-link and the field currents. A transient curve of the current rising can be shaped by utilizing an integrator to gradually eliminate the error between instantaneous and steady-state estimated values:

$$i_{\mathrm{dc.est}} = \int k_{i_\mathrm{dc}} \cdot (i_{\mathrm{dc.end.est}} - i_{\mathrm{dc.est}}) \cdot dt, \qquad (19)$$

$$i_{\mathrm{f.est}} = \int k_{i_\mathrm{f}} \cdot (i_{\mathrm{f.end.est}} - i_{\mathrm{f.est}}) \cdot dt, \qquad (20)$$

where $i_{\mathrm{dc.est}}$ is the instantaneous dc-link current estimation, $i_{\mathrm{dc.end.est}}$ is the steady-state dc-link current estimation, $k_{i_\mathrm{dc}}$ is the gain of the dc-link current shaping integration, $i_{\mathrm{f.est}}$ is the instantaneous field current estimation, $i_{\mathrm{f.end.est}}$ is the steady state field current estimation, and $k_{i_\mathrm{f}}$ is the gain of the field current shaping integration. Then, the field winding temperature can be estimated as follows:

$$T_{\mathrm{f.est}} = \int k_{T_\mathrm{f}} \cdot \left(i_{\mathrm{dc.avg}} - i_{\mathrm{dc.est}}\right) \cdot dt + T_{\mathrm{f.intial.est}}, \qquad (21)$$

where $T_{\mathrm{f.intial.est}}$ is the initial guess of the field winding temperature. $T_{\mathrm{f.est}}$ is clamped within 0°C and 200°C to avoid possible error.

### E. Simulation

The algorithm is tested by performing a sequence of duty cycles, as shown in Fig. 9. The duty cycle ramps from 0 up to 1.0 at 0.5 s and ramps down to 0.5 at 2.5 s. At 4.5 s, it ramps to 1.0; at 6.5 s, it ramps down to 0.5 again.

A thermal model is implemented to describe the adiabatic process of the field winding as shown in Fig. 10. The copper loss of the field winding can be calculated as follows:

$$p_\mathrm{f} = {i_\mathrm{f}}^2 \cdot R_\mathrm{f}, \qquad (22)$$

where $p_\mathrm{f}$ is the instantaneous field copper loss and $i_\mathrm{f}$ is the instantaneous field current. Using a thermal capacitance $C_{\mathrm{th.f}}$ of 360 J/K, the field winding temperature can be calculated by integration of the copper loss

$$T_\mathrm{f} = \int \frac{p_\mathrm{f}}{C_{\mathrm{th.f}}} \cdot dt = \frac{R_\mathrm{f}}{C_{\mathrm{th.f}}} \cdot \int {i_\mathrm{f}}^2 \cdot dt. \qquad (23)$$

The thermal model used here is to introduce temperature variations to verify the dynamic tracking capability of the estimation algorithm instead of accurately describing the thermal characteristics of the machine. Sequences of duty cycles with variable temperatures are also performed. Cases of different starting temperatures are simulated, and the case of a temperature starting at 30°C is shown in Fig. 11. The initial

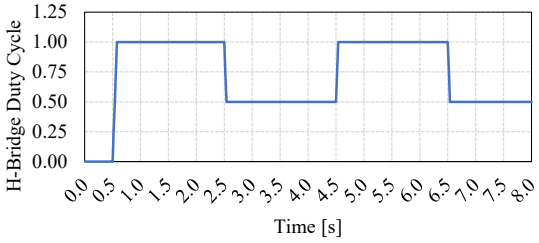


Fig. 9. Duty cycle sequence test.

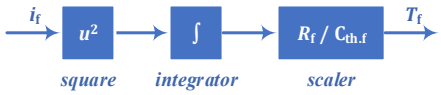


Fig. 10. Model describing the adiabatic process of the field winding.

value of the temperature estimation is 40°C, and after the algorithm is activated at 0.5 s, the algorithm starts to eliminate the temperature estimation error. From Fig. 11 (c), it can be observed that the dc-link current estimation, as the algorithm feedback, closely follows the real dc-link current. This verifies the functionality of the integrator in the dynamic response shaping process. The temperature estimation in Fig. 11 (b) shows that the trend of the estimated temperature closely follows the trend of the real temperature. Errors due to the accuracy of linear interpolation (lookup table, by the subscript denoted TAB) and curve fitting (denoted by the subscript CF) exist. The tracking, which uses curve fitting, provides a slightly larger error than linear interpolation, since curve fitting is an approximation of the curve. Spikes are observed at duty cycle steps. This is due to the error between the estimated and the real dc-link current during the transients. The dynamic response shaping process helps in reducing the spikes. The field current estimation closely follows the real value as shown in Fig. 11 (a) due to the successful estimation of the dc-link current and the field winding temperature. The zoomed-in details of the field current estimation during the duty cycle steps are shown in Fig. 11 (d)-(g). In general, the differences between the estimated and the real curves are minor during both the rise and fall of the field current.

### *F. Experimental Results*

The same duty cycle sequence is performed to experimentally verify the algorithm as shown in Fig. 9. The winding temperature starts at 30°C in Fig. 12 and at 100°C in Fig. 13 respectively. Due to a limited number of digital to analogue converter (DAC) channels in DSP, only the field current and field winding temperature estimation curves are extracted. In a similar way as used in the simulation, the initial temperature estimation is set at 40°C and the algorithm starts after its activation at 0.5 s. The temperature is measured by two PT100 sensors and is also roughly calculated using the ratio between the field voltage and the field current.

The estimated and the real field currents are compared in Fig. 12 (a) and the zoomed-in curves are shown in Fig. 12 (c)-(f). In general, the estimated current closely follows the real

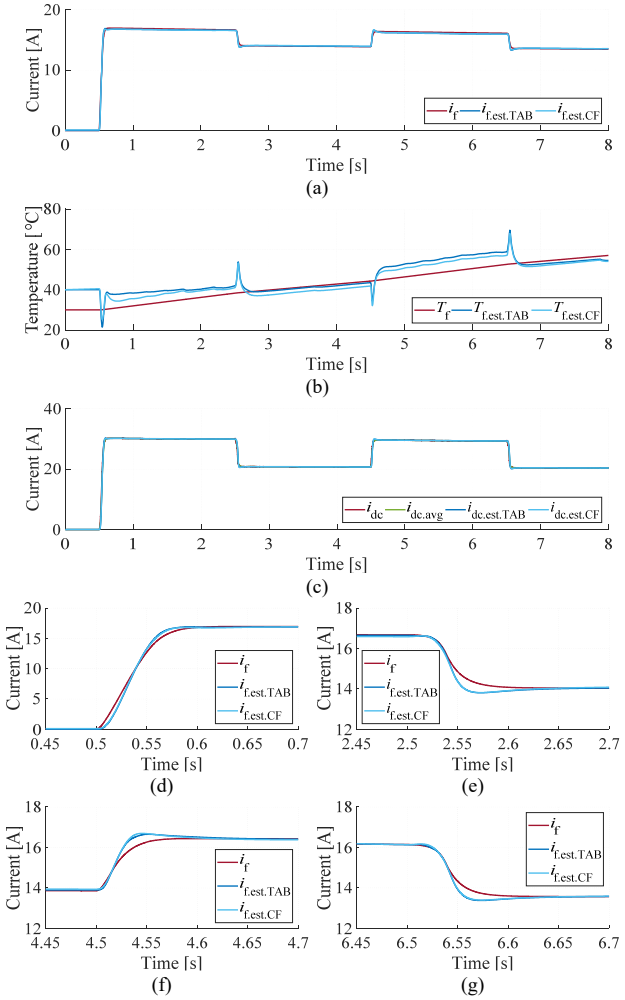


Fig. 11. Current and temperature tracking (simulation at 30°C).
(a) field current from 0 to 8 s; (b) field winding temperature from 0 to 8 s;
(c) DC-link current from 0 to 8 s;
(d) field current from 0.45 to 0.70 s; (e) field current from 2.45 to 2.70 s;
(f) field current from 4.45 to 4.70 s; (g) field current from 6.45 to 6.70 s.

current. In the 100°C case, an overshoot of the field current estimation occurs at 0.5 s, as shown in Fig. 13 (a). This is due to the huge gap between the initial temperature assumption and the real temperature value. The current estimation error is then eliminated as the temperature estimation closely tracks the real one.

It can be observed that the estimation error is higher at 0.5 duty cycle than at 1.0 duty cycle. This can be explained by observing Fig. 6. At a lower duty cycle, the differences between the curves are smaller. Since the algorithm utilizes the difference between dc-link currents at different temperatures as the feedback to correct the temperature estimation, a smaller difference of the dc-link currents makes the temperature estimation more difficult. Analytically, an increase in the temperature results in an increase in $R_f$. From the analytical solution shown in (17), the difference in the dc-link current can be expressed as follows:

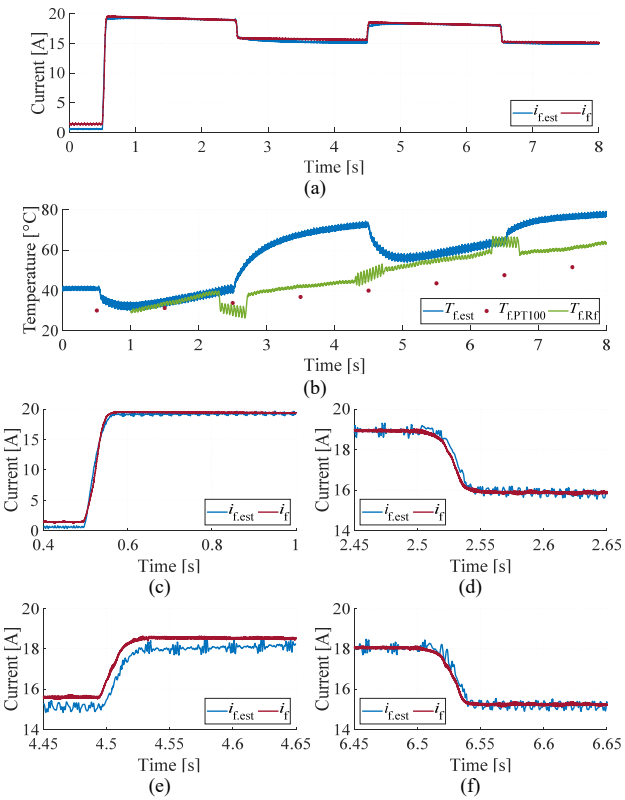


Fig. 12. Current and temperature tracking (experiment at 30°C).
(a) field current from 0 to 8 s; (b) field winding temperature from 0 to 8 s;
(c) field current from 0.40 to 1.00 s; (d) field current from 2.45 to 2.65 s;
(e) field current from 4.45 to 4.65 s; (f) field current from 6.45 to 6.65 s.

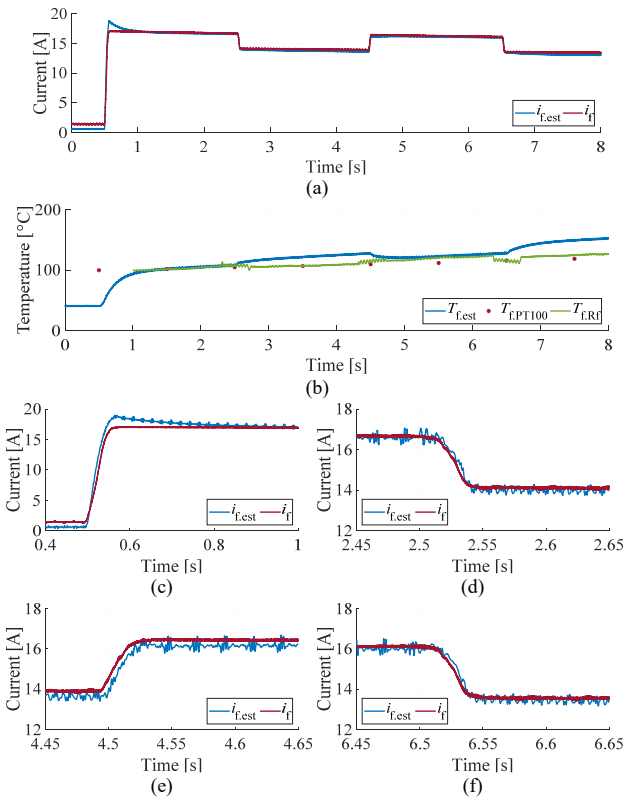


Fig. 13. Current and temperature tracking (experiment at 100°C).
(a) field current from 0 to 8 s; (b) field winding temperature from 0 to 8 s;
(c) field current from 0.40 to 1.00 s; (d) field current from 2.45 to 2.65 s;
(e) field current from 4.45 to 4.65 s; (f) field current from 6.45 to 6.65 s.

$$\Delta I_{dc} \propto \frac{1-\cos(\pi d)}{R_{f.1} \cdot R_{f.2}} \cdot (R_{f.2} - R_{f.1}), \qquad (24)$$

where $R_{f.1}$ and $R_{f.2}$ are the resistances at different temperatures. The term $\frac{1-\cos(\pi d)}{R_{f.1} \cdot R_{f.2}}$ can be regarded as an amplification factor of the resistance difference $(R_{f.2} - R_{f.1})$. Therefore, a higher duty cycle results in a higher amplification factor $\frac{1-\cos(\pi d)}{R_{f.1} \cdot R_{f.2}}$ and in a higher $\Delta I_{dc}$. This is the reason why a higher duty cycle exhibits better resolution for the temperature estimation.

## IV. Closed-Loop Field Current Control

### A. Control Algorithm

With the field current estimation, it becomes possible to apply closed-loop control to the field current. The schematic diagram of the algorithm is shown in Fig. 14. Initially, the field current error $i_{f.err}$ is calculated by comparing the reference value $i_{f.ref}$ with the estimated value $i_{f.est}$:

$$i_{f.err} = i_{f.ref} - i_{f.est}. \qquad (25)$$

The error is then squared and amplified by a scale factor $k_{ctrl}$:

$$d_{H.unlim} = \int k_{ctrl} \cdot \text{sign}(i_{f.err}) \cdot {i_{f.err}}^2 \cdot dt, \qquad (26)$$

where $d_{H.unlim}$ is the unlimited duty cycle and it is clamped between 0 and 1 to become $d_{H.lim}$. The square is used to adjust the duty cycle in big steps when the error is large and in small steps when the error decreases. In this work, $k_{ctrl}$ is selected by considering the field current versus the duty cycle profile as well as the step size of the digital processor. The control bandwidth is limited by the dynamic sharping process and the moving average filter of the estimator. The bandwidth of the dynamic sharping process is decided by the gain $k_{i_{dc}}$, $k_{i_f}$ and $k_{T_f}$. Nevertheless, if other techniques are adopted to deal with EMI, the limitation of moving average does not exist. In addition, during fault conditions of the machine, the power will be directly cutoff instead of ramping down the field current reference as shown in this work.

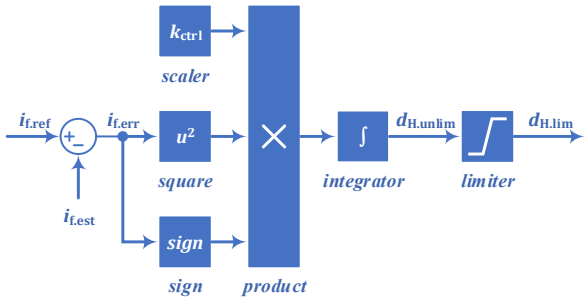


Fig. 14. Closed-loop field current control.

### B. *Experimental Results*

The field current reference ramps from 0 A up to 18 A at 0.5 s and ramps down to 12 A at 2.5 s. At 4.5 s, it ramps to 18 A; at 6.5 s, it ramps down to 12 A again. Experimental results, which start at 30°C, are presented in Fig. 15. The current reference $i_{\mathrm{f.ref}}$ and the current estimation $i_{\mathrm{f.est}}$ are the outputs from the DAC of the DSP, whereas the real current $i_{\mathrm{f}}$ is measured using a current probe. It is observed that the real current closely follows the reference current.

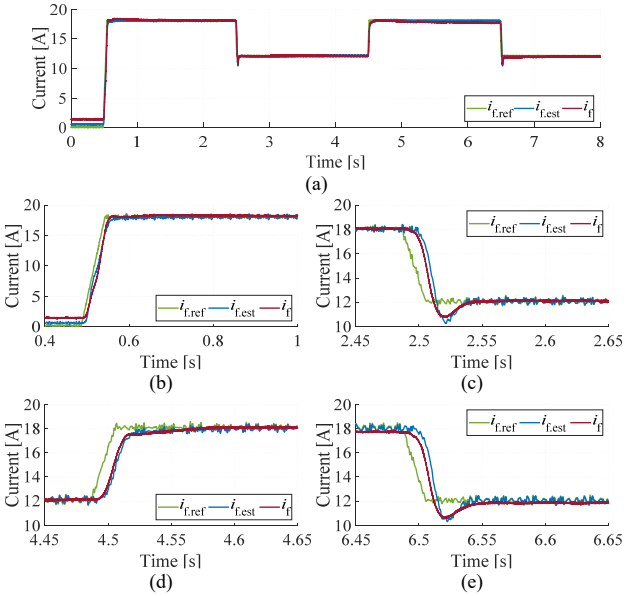


Fig. 15. Closed-loop field current control (experiment at 30°C).
(a) field current from 0 s to 8 s;
(b) field current from 0.40 s to 1.00 s; (c) field current from 2.45 s to 2.65 s;
(d) field current from 4.45 s to 4.65 s; (e) field current from 6.45 s to 6.65 s.

The real current lags the reference by less than 10 ms and it rises from 0 A to 18 A within 50 ms. The steady state error of the field current control

$$\left|\frac{I_{\mathrm{f.ref}} - I_{\mathrm{f}}}{I_{\mathrm{f.ref}}}\right| \times 100\%, \tag{27}$$

is below 2% in this case.

Experimental results, which start at 100°C, are presented in Fig. 16. The current reference applied here is the same as in the 30°C test. It is observed that at 100°C, the field current cannot reach 18 A even with duty cycle 1.0, due to the increase of resistance. Hence when an 18 A reference is applied, a gap always exists between the real field current and the reference current. The gap gradually becomes larger, since the temperature increases during the test. During the transients at around 0.5 s, the field current is temporarily overestimated because the estimator needs some time to catch up with the real temperature. The temperature estimation keeps updating until around 1.0 s and the current estimation comes back to the real value. Except for the time intervals with an 18 A reference, when the power transfer capability is exceeded, the steady-state error of the field current control is below 1.5% in this case. This shows that even in the scenario when the output is

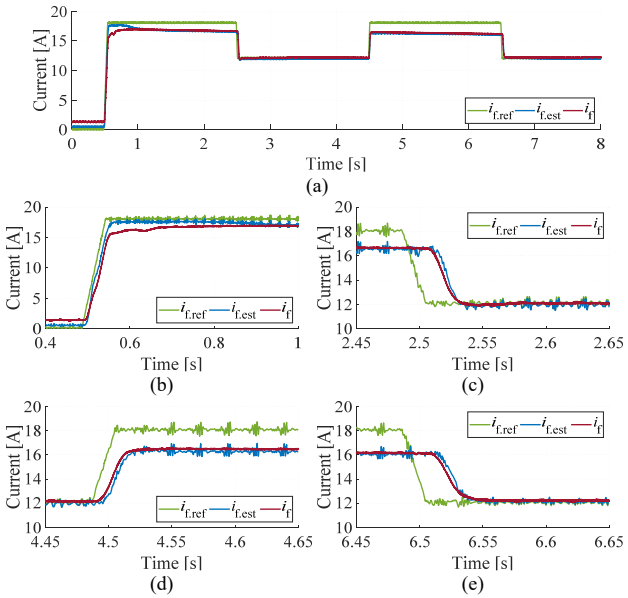


Fig. 16. Closed-loop field current control (experiment at 100°C).
(a) field current from 0 s to 8 s;
(b) field current from 0.40 s to 1.00 s; (c) field current from 2.45 s to 2.65 s;
(d) field current from 4.45 s to 4.65 s; (e) field current from 6.45 s to 6.65 s.

saturated, the estimation of field current can still work, and when the reference current becomes possible for the circuit to reach, the field current starts to follow the reference again.

## V. Estimation and Control with Machine Rotating

To validate the estimation algorithm and the field current control in real operation, the machine was then assembled, and the performance of the machine, including torque, efficiency and displacement power factor (DPF) are compared with the expected values obtained from finite element method (FEM) calculations.

### A. *Field Current Ripple Due to Airgap Permeance Variation*

When the machine is in operation, the effective airgap permeance will vary as the rotor poles move past the stator teeth. Then the flux linkage of the field winding will fluctuate, and an EMF will be induced in the field winding. The induced EMF will cause a current ripple consequently, and the current ripple will further tend to cancel the flux variation in return according to Lenz's law. In the end, the variations of current and flux will come to a balanced level in steady state. The ripple component of field current $I_{\mathrm{f.ripple}}$ in steady state can be formulated as

$$I_{\mathrm{f.ripple}} = \frac{|E_{\mathrm{f.ripple}}|}{|R_{\mathrm{f}} + jX_{\mathrm{f}}|} = \frac{h\omega_{\mathrm{r}}\psi_{\mathrm{f.ripple}}}{|R_{\mathrm{f}} + jh\omega_{\mathrm{r}}L_{\mathrm{f}}|}, \tag{28}$$

where $E_{\mathrm{f.ripple}}$ and $\psi_{\mathrm{f.ripple}}$ are the induced voltage and flux linkage in the field winding due to airgap permeance variation, $X_{\mathrm{f}}$ is the field winding reactance at the ripple frequency, $h$ is the harmonic order of the field current ripple and $\omega_{\mathrm{r}}$ is the electrical speed of the machine.

The harmonic order of the field current ripple $h$ should be equal to the number of teeth per pole pair

$$h = 2mq, \tag{29}$$

where $m$ is the number of phases, $q$ is the number of slots per pole per phase. If $q$ increases, $h$ will increase, whereas the harmonic amplitude will decrease because the flux passing through each tooth becomes minor compared with the main flux. In addition, when the machine speed increases, the harmonic frequency will increase. However, in most cases, the inductance of an EESM field winding is quite large, and therefore, the reactance at the ripple frequency is much larger than the resistance in the field winding

$$X_{\mathrm{f}} = h\omega_{\mathrm{r}}L_{\mathrm{f}} \gg R_{\mathrm{f}}. \tag{30}$$

In this case, (28) becomes

$$I_{\mathrm{f.ripple}} \approx \frac{\psi_{\mathrm{f.ripple}}}{L_{\mathrm{f}}}, \tag{31}$$

which means the amplitude of current ripple is independent from the machine speed.

To verify this, the current variations under no-load condition are calculated in FEM analysis. The field winding is powered from a dc voltage source. The cases with average field current at 5, 10 and 15 A and speed at 1500 and 6000 rpm are presented in Fig. 17. 360 steps are calculated in each electrical cycle. The peak-to-peak values of current ripple versus the average values are 1.8%, 5.0% and 9.1% for each average current level respectively at both 1500 rpm and 6000 rpm. As can be noticed, the current variations are independent from the machine speed.

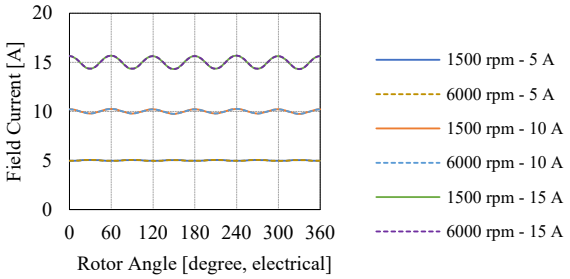


Fig. 17. Field current ripple due to airgap permeance variations at 1500 and 6000 rpm.

The peak-to-peak values of field current ripple in percentage versus the average values are presented in Fig. 18. The current averages are presented in logarithm from 1 A to 10000 A. At low average current levels, the current ripples are small. This is because the flux is weak and thus the flux available to fluctuate is limited. As the current average increases, the flux variation increases and consequently the current ripple increases. However, if the field current increases even further, the ripple will decrease. This is because the iron-core is then totally saturated and there is no difference between iron-core and air in permeability. Hence the permeance variation becomes minor and the current ripple decreases.

In this study, laminations are used to build the rotor iron core. In case solid iron is used, then eddy currents will be induced on the rotor surface due to flux variation. The eddy currents will further cancel the flux variations. Consequently, the ripple of field current will become even lower.

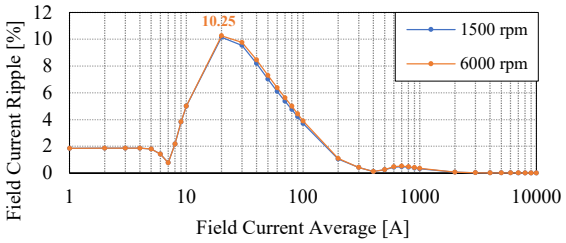


Fig. 18. Field current ripple in percentage due to effective airgap permeance variations at 1500 and 6000 rpm.

## B. *Experimental Setup*

The experimental setup is presented in Fig. 19 . The EESM is connected to a load machine through a torque sensor Lorenz DR-2512 as shown in (a). The stator winding is powered from a three-phase inverter while the brushless excitation system is powered from an H-bridge converter. The control station is shown in (b). The load machine is controlled through a LabView program while the EESM is controlled through a Texas Instrument digital signal processor TMS320F28379D.

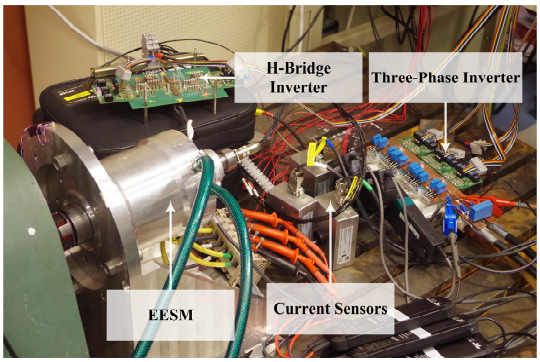


(a)

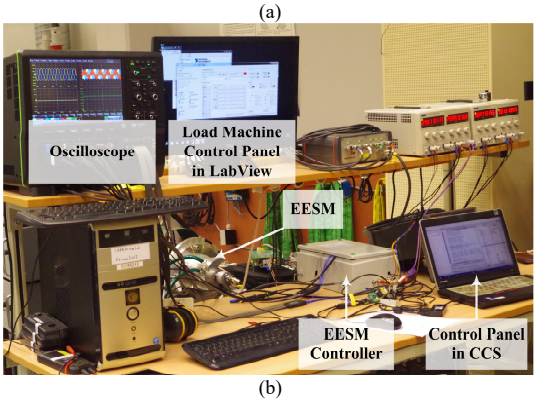


(b)

Fig. 19. Experimental setup to validate the estimation algorithm and control during machine operation. (a) test bench. (b) control station.

### C. *Experimental Results*

To check the effects from airgap permeance variation, the currents are measured during machine operations. The waveforms of the dc-link input current to H-bridge inverter and the three-phase stator currents are presented in Fig. 20 (a) and (c) respectively. Fast Fourier transform (FFT) is also performed and the results are shown in (b) and (d) respectively. The machine rotates at 750 rpm in this test. The three-phase stator currents are at 442.5 A as the amplitude while the estimated field current is at 15 A. As can be noticed, the sixth order harmonic at 300 Hz of the dc-link input current to H-bridge inverter is minor. Since the estimation algorithm is based on the dc-link input current to the H-bridge inverter, this means that the algorithm is not disturbed by the effective airgap permeance variation.

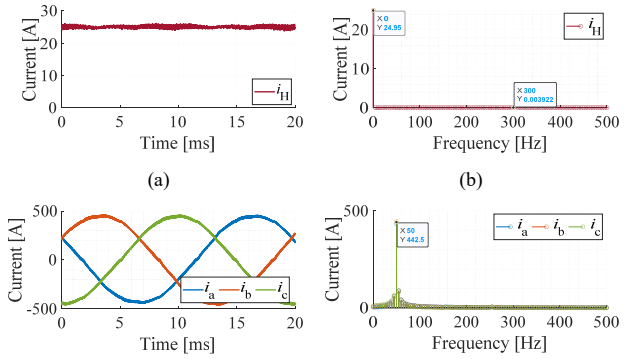


Fig. 20. Current measurements in load condition at 750 rpm. (a) dc-link input current to H-bridge inverter. (b) FFT of dc-link input current to H-bridge inverter. (c) three-phase stator currents. (d) FFT of three-phase stator currents.

The torque output, efficiency and DPF of the machine are compared with FEM results in Fig. 21. The field current ranges from 5 A to 15 A in a step of 5 A, while the q-axis current ranges from 100 A to 500 A in a step of 100 A. The d-axis current is set to 0 A. The machine rotates at 750 rpm in this test. The torque transducer measurements are presented in (a). As can be seen, the measurements closely follow the FEM results. The efficiency and DPF are presented in (b) and (c). Only the fundamental components of voltage and current are considered in the DPF calculation. Generally, the measurements of efficiency and DPF match the FEM calculations quite well. This indicates that the estimation algorithm and the closed-loop control work as expected.

## VI. Conclusions

In this paper, an algorithm is proposed to estimate the current and temperature of the field winding in electrically excited synchronous machines with high-frequency brushless exciters. The dc-link current is utilized as the feedback to correct the estimation error. Simulations and experiments were performed to verify the algorithm. The temperature and current curves estimated by the algorithm closely follow the real temperature and current curves in both simulations and

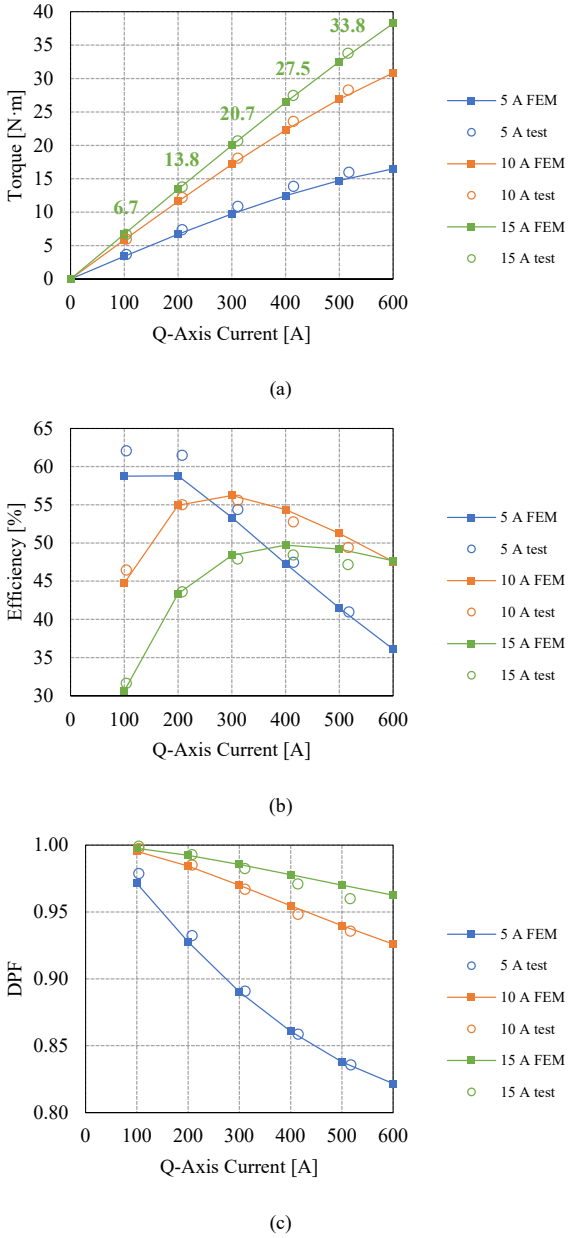


Fig. 21. Results of machine performance from FEM calculations and tests at 750 rpm. (a) torque. (b) efficiency. (c) displacement power factor.

experiments. It was shown that the resolution of the temperature estimation is related to the duty cycle. Specifically, a higher duty cycle provides a higher resolution and vice versa. Based on the proposed estimation algorithm, a closed-loop field current control was implemented as a further step in this work. In general, the stead-state error of the control is below 2%. It is verified in experiments that the estimator successfully supports the field current control. The proposed algorithm is practical and reliable for the estimation of the field winding temperature and current. With the assistance of this algorithm, dynamic control of the field current becomes possible.

## VII. References


[1] D. G. Dorrell, A. M. Knight, M. Popescu, L. Evans and D. A. Staton, "Comparison of Different Motor Design Drives for Hybrid Electric Vehicles," in *2010 IEEE Energy Conversion Congress and Exposition*, Atlanta, 2010.

[2] J. D. Widmer, R. Martin and M. Kimiabeigi, "Electric Vehicle Traction Motors without Rare Earth Magnets," *Sustainable Materials and Technologies,* vol. 3, pp. 7-13, 2015.

[3] K. Binnemans, P. T. Jones, B. Blanpain, T. V. Gerven, Y. Yang, A. Walton and M. Buchert, "Recycling of Rare Earths: A Critical Review," *Journal of Cleaner Production,* vol. 51, pp. 1-22, 2013.

[4] L. Huang, Z. Zhu and W. Chu, "Optimization of Electrically Excited Synchronous Machine for Electrical Vehicle Applications," in *Machines and Drives (PEMD 2016), 8th IET International Conference on Power Electronics*, Glasgow, UK, 2016.

[5] J. Tang and Y. Liu, "Design and Experimental Verification of a 48 V 20 kW Electrically Excited Synchronous Machine for Mild Hybrid Vehicles," in *2018 XIII International Conference on Electrical Machines (ICEM)*, Alexandroupoli, 2018.

[6] J. Tang and Y. Liu, "Comparison of Copper Loss Minimization and Field Current Minimization for Electrically Excited Synchronous Motor in Mild Hybrid Drives," in *19th European Conference on Power Electronics and Applications (EPE'17 ECCE Europe)*, Warsaw, Poland, 2017.

[7] J. Choi, I. Jeong, K. Nam and S. Jung, "Sensorless control for electrically energized synchronous motor based on signal injection to field winding," in *IECON 2013 - 39th Annual Conference of the IEEE Industrial Electronics Society*, Vienna, Austria, 2013.

[8] J. K. Nøland, S. Nuzzo, A. Tessarolo and E. F. Alves, "Excitation System Technologies for Wound-Field Synchronous Machines: Survey of Solutions and Evolving Trends," *IEEE Access,* vol. 7, pp. 109699 - 109718, 2019.

[9] E. M. Illiano, "Design of a Highly Efficient Brushless Current Excited Synchronouos Motor for Automotive Purposes," Swiss Federal Institute of Technology in Zurich (ETH Zurich), Zurich, 2014.

[10] E. M. Illiano, "Design of a Brushless Separately Excited Synchronous Motor," BRUSA Elektronik AG, Sennwald, 2014.

[11] C. Stancu, T. Ward, K. M. Rahman, R. Dawsey and P. Savagian, "Separately Excited Synchronous Motor With Rotary Transformer for Hybrid Vehicle Application," *IEEE Transactions on Industry Applications,* vol. 54, no. 1, pp. 223-232, 2018.

[12] Y. Liu, D. Pehrman, O. Lykartsis, J. Tang and T. Liu, "High frequency exciter of electrically excited synchronous motors for vehicle applications," in *2016 XXII International Conference on Electrical Machines (ICEM)*, Lausanne, Switzerland, 2016.

[13] J. Tang and Y. Liu, "Study of Voltage Spikes and Temperature Rise in Power Module Based Integrated Converter for 48 V 20 kW Electrically Excited Synchronous Machines," in *APEC 2018*, San Antonio, Taxes, USA, 2018.

[14] M. Tosi, "Rotary Transformer Design for Brushless Electrically Excited Synchronous Machines," University of Padua, Padua, 2014.

[15] T. Raminosoa and R. Wiles, "Contactless Rotor Excitation for Traction Motors," in *2018 IEEE Energy Conversion Congress and Exposition (ECCE)*, Portland, 2018.

[16] Y. Luan, B. Lin, X. Ma and X. Zhu, "Innovative Contactless Energy Transfer Accessory for Rotary Ultrasonic Machining and Its Circuit Compensation Based on Coil Turns," *IEEE Transactions on Industrial Electronics,* vol. 64, no. 10, pp. 7810 - 7818, 2017.

[17] N. Jiao, W. Liu, Z. Zhang, T. Meng, J. Peng and Y. Jiang, "Field Current Estimation for Wound-Rotor Synchronous Starter–Generator With Asynchronous Brushless Exciters," *IEEE Transactions on Energy Conversion,* vol. 32, no. 4, pp. 1554 - 1561, 2017.

[18] J. Dai, S. Hagen, D. C. Ludois and I. P. Brown, "Synchronous Generator Brushless Field Excitation and Voltage Regulation via Capacitive Coupling Through Journal Bearings," *IEEE Transactions on Industry Applications,* vol. 53, no. 4, pp. 3317 - 3326, 2017.

[19] S.-B. Lee, T. G. Habetler, R. G. Harley and D. J. Gritter, "An Evaluation of Model-Based Stator Resistance Estimation for Induction Motor Stator Winding Temperature Monitoring," *IEEE Transactions on Energy Conversion,* vol. 17, no. 1, pp. 7 - 15, 2002.

[20] S.-B. Lee and T. G. Habetler, "An Online Stator Winding Resistance Estimation Technique for Temperature Monitoring of Line-Connected Induction Machines," *IEEE Transactions on Industry Applications,* vol. 39, no. 3, pp. 685 - 694, 2003.

[21] D. D. Reigosa, J. M. Guerrero, A. B. Diez and F. Briz, "Rotor Temperature Estimation in Doubly-Fed Induction Machines Using Rotating High-Frequency Signal Injection," *IEEE Transactions on Industry Applications,* vol. 53, no. 4, pp. 3652 - 3662, 2017.

[22] K.-R. Cho and J.-K. Seok, "Induction Motor Rotor Temperature Estimation Based on a High-Frequency Model of a Rotor Bar," *IEEE Transactions on Industry Applications,* vol. 45, no. 4, pp. 1267 - 1275, 2009.

[23] J. Tang, Y. Liu and N. Sharma, "Modeling and Experimental Verification of High-Frequency Inductive Brushless Exciter for Electrically Excited Synchronous Machines," *IEEE Transactions on Industry Applications,* vol. 55, no. 5, pp. 4613 - 4623, 2019.

[24] R. L. Steigerwald, "A Comparison of Half-Bridge Resonant Converter Topologies," *IEEE Transactions on Power Electronics,* vol. 3, no. 2, pp. 174 - 182, 1988.


## VIII. Biographies

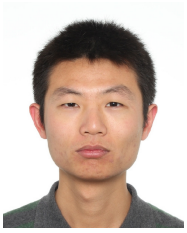

**Junfei Tang** (S'16) received the B.Eng. degree in electrical engineering from Jiangsu University, Zhenjiang, China, in 2013, and the M.Sc and licentiate degrees in electric power engineering from Chalmers University of Technology, Gothenburg, Sweden, in 2016 and 2019 respectively. Now he is pursuing his doctoral degree in electric machines and power electronics in Chalmers University of Technology.

**Yujing Liu** (SM'12) received the B.Sc., M.Sc. and Ph.D. degrees in electrical engineering from Harbin Institute of Technology, Harbin, China, in 1982, 1985, and 1988, respectively. In 1996-2013, he worked in ABB Corporate Research, Västerås, Sweden. Since 2013, he is a professor on electrical power engineering in Chalmers University of Technology. Gothenburg, Sweden. His interest includes research on motors, converters, and wireless charging for electric vehicles, generators and power electronics for tidal power conversion, and high efficiency machines for energy saving in industrial applications. Yujing Liu is a senior IEEE member and a member in Swedish Standard Committee on Electrical Machines.

**Stefan Lundberg** (S'04–M'06) received the Ph.D. degree in electrical engineering from Chalmers University of Technology, Gothenburg, Sweden, in 2007. He is with the Division of Electric Power Engineering, Chalmers University of Technology. His main area of interest is control and modeling of wind parks.